Research Square

Preprints are preliminary reports that have not undergone peer review.
They should not be considered conclusive, used to inform clinical practice,
or referenced by the media as validated information.

Effect of Metal Transfer Mode on Local Chemical Inhomogeneity in Dual-Wire Electron Beam Additive Manufacturing of Nitinol

Alexander Vladimirovich Nekhoroshev

NekhoroshevAV@mpei.ru

Moscow Power Engineering Institute: Nacional'nyj issledovatel'skij universitet MEI
https://orcid.org/0009-0000-3719-9509

Alexey Sergeevich Pankov

Perm National Research Polytechnic University: Permskij nacional'nyj issledovatel'skij politehniceskij universitet

Alexey Vitalyevich Glinskiy

Moscow Power Engineering Institute: Nacional'nyj issledovatel'skij universitet MEI

Roman Pozolovich Davlyatshin

Perm National Research Polytechnic University: Permskij nacional'nyj issledovatel'skij politehniceskij universitet

Alexey Leonidovich Goncharov

Moscow Power Engineering Institute: Nacional'nyj issledovatel'skij universitet MEI

Dmitry Nikolaevich Trushnikov

Perm National Research Polytechnic University: Permskij nacional'nyj issledovatel'skij politehniceskij universitet

Ivan Sergeevich Chulkov

Moscow Power Engineering Institute: Nacional'nyj issledovatel'skij universitet MEI

Nikita Pavlovich Chernyshev

Perm National Research Polytechnic University: Permskij nacional'nyj issledovatel'skij politehniceskij universitet

Research Article

Keywords: additive technologies, additive shaping, electron beam, electron beam welding, vacuum surfacing, multi-wire surfacing, nitinol, mathematical modelling, smoothed particle hydrodynamics

Posted Date: October 9th, 2026

DOI: https://doi.org/10.21203/rs.3.rs-10823965/v1

License: This work is licensed under a Creative Commons Attribution 4.0 International License.
Read Full License

Effect of Metal Transfer Mode on Local Chemical Inhomogeneity in Dual-Wire Electron Beam Additive Manufacturing of Nitinol

Alexander Vladimirovich Nekhoroshev[1*], Alexey Sergeevich Pankov[2], Alexey Vitalyevich Glinskiy[1], Roman Pozolovich Davlyatshin[2], Alexey Leonidovich Goncharov[1], Dmitry Nikolaevich Trushnikov[2], Ivan Sergeevich Chulkov[1], Nikita Pavlovich Chernyshev[2]

[1] National Research University "Moscow Power Engineering Institute" (MPEI), 111250, Moscow, Russia
[2] Perm National Research Polytechnic University (PNRPU), 614990, Perm, Russia
*Corresponding author. Email: NekhoroshevAV@mpei.ru

Abstract.

Local chemical inhomogeneities are the primary obstacle to producing NiTi shape memory alloys with reproducible functional properties by dual-wire electron beam additive manufacturing (EBAM). This study investigates the mechanisms of their formation and identifies the technological conditions for their suppression. Using smoothed particle hydrodynamics (SPH) simulation, high-speed videography, and metallographic analysis, the convergence angle β of the wire feed nozzles was found to be the key parameter controlling the metal transfer mode. At $\beta \geq 30°$, droplet transfer of the nickel wire was observed, caused by the difference in surface tension coefficients of liquid nickel and titanium, resulting in asynchronous delivery of components to the melt pool and formation of zones with disrupted stoichiometry. At $\beta = 15°$, mixing was governed solely by the electron beam deflection pattern through two separate transfer bridges. At parallel wire feeding ($\beta = 0°$), component mixing began prior to entry into the melt pool, forming a single stable transfer bridge. Optical flow analysis of high-speed recordings showed that at $\beta = 0°$ the time margin for convective homogenisation reaches ~67% compared to ~7% at $\beta = 30°$. The mean deviation of the chemical composition coefficient γ from the target value decreased from 3.6% at $\beta = 30°$ to 0.4% at $\beta = 0°$. Metallographic analysis confirmed a uniform NiTi matrix and homogeneous hardness distribution (358–385 HV5) in samples produced at $\beta = 0°$.

Keywords: additive technologies, additive shaping, electron beam, electron beam welding, vacuum surfacing, multi-wire surfacing, nitinol, mathematical modelling, smoothed particle hydrodynamics.

Acknowledgements

The research was supported by the Ministry of Science and Higher Education of the Russian Federation: at the National Research University "Moscow Power Engineering Institute" (MPEI) under State Assignment No. FSWF-2026-0004 "Development of a scientifically grounded methodology for designing the blade apparatus of advanced high-power turbomachines based on the application of functionally graded materials and coatings", and at Perm National Research Polytechnic University (PNRPU) under State Assignment No. FSNM-2024-0003 "Development of scientific and technological foundations for the formation of a material-structure system with special properties based on hybrid additive technologies".

1. Introduction

Nitinol is one of the most sought-after functional materials in aerospace and energy industries due to its unique combination of shape memory effect and superelasticity [1, 2]. However, the properties of nitinol are highly sensitive to chemical composition: a variation of 0.1 wt.% in nickel content shifts the phase transformation temperatures by 6–10°C [3], making precise composition control a critical requirement for achieving the desired functional characteristics. Conventional nitinol production methods — vacuum induction melting and electron beam melting

followed by mechanical processing — provide the required compositional accuracy but are associated with high production costs and limited capability for near-net-shape fabrication of complex components [4, 5].

A promising alternative approach is dual-wire electron beam additive manufacturing (EBAM), in which nitinol is synthesised in-situ during layer-by-layer deposition by co-melting nickel and titanium filler wires with an electron beam in vacuum [6, 7]. This approach combines metallurgical synthesis and near-net-shape fabrication in a single process, substantially reducing production costs. Several studies have confirmed the feasibility of nitinol synthesis by this method, demonstrating the formation of the NiTi phase and functional properties [8–10].

However, in practice, dual-wire EBAM of nitinol inevitably produces local chemical inhomogeneities — zones with elevated nickel or titanium content relative to the stoichiometric composition. In such zones, brittle intermetallic phases Ti_2Ni, $TiNi_3$ and their metastable derivatives form, reducing material ductility, suppressing martensitic transformations and compromising the functional properties of nitinol [11, 12].

The local chemical composition of the synthesised material is determined not only by the ratio of nickel and titanium wire feed rates, but also by the melting behaviour and metal transfer mode into the melt pool. When the components enter the pool asynchronously, individual regions may be temporarily enriched in nickel or titanium, and subsequent convective mixing does not always ensure complete homogenisation prior to solidification. Thus, the metal transfer mode from the filler wires is one of the factors governing the formation of local chemical inhomogeneity.

The transfer mode, in turn, depends on the conditions of filler wire interaction with the electron beam and the melt pool, including the wire feeding geometry. However, the influence of the feeding geometry of dissimilar wires on the nickel and titanium transfer behaviour and the subsequent formation of local chemical inhomogeneity in dual-wire EBAM of nitinol has not been systematically investigated.

Mathematical modelling is one of the most effective tools for studying melt pool hydrodynamics and metal transfer mechanisms. Unlike physical experiments, which require significant time and material resources, numerical simulation enables investigation of process parameter effects on melt flow behaviour and component distribution at the design stage, without conducting a series of costly experiments. For describing free surface dynamics and mixing of dissimilar liquid metals, smoothed particle hydrodynamics (SPH) has demonstrated particular effectiveness, enabling simulation of large free surface deformations, droplet and bridge formation [13, 14]. Combined with experimental verification via high-speed videography, this approach makes it possible to establish the physical mechanism of inhomogeneity formation and to select a wire feeding configuration that minimises their occurrence.

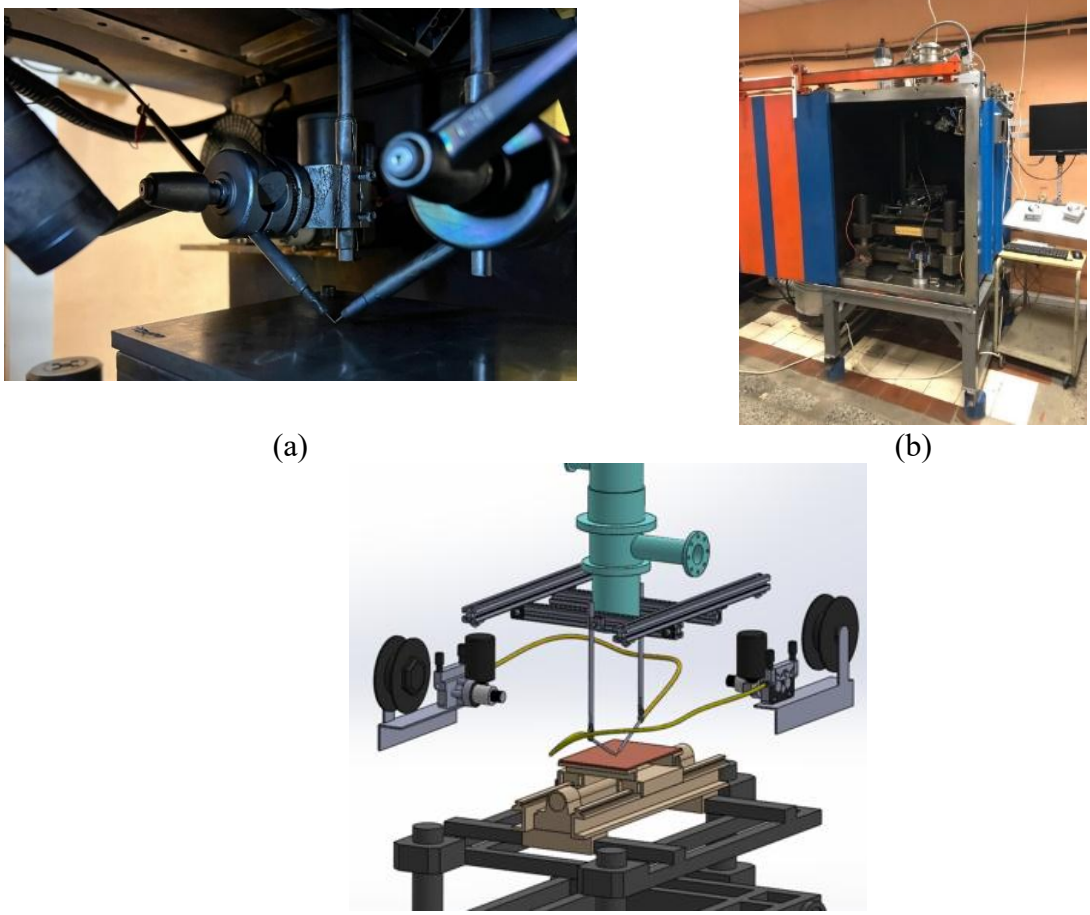
The aim of this study is to establish the mechanisms of local chemical inhomogeneity formation in dual-wire electron beam additive manufacturing of nitinol and to formulate, on this basis, technological approaches for ensuring a homogeneous chemical composition of the synthesised alloy.

2. Research methodology

2.1. Experimental setup for dual-wire electron beam additive manufacturing

Experiments were conducted on a test bench based on the ELA-15 electron beam complex equipped with a 1 m^3 vacuum chamber and a stationary electron beam gun with a power of 15 kW. Nickel wire NP2 DKRNT and titanium wire VT1-00sv with a diameter of 1 mm were used as filler materials. Deposition was performed onto a nitinol substrate of grade TN-1K.

The setup is equipped with two independent wire feed mechanisms driven by 120 W DC motors and specially designed nozzles mounted on adjustable holders, enabling positioning within an angular range of 0°–90° relative to the substrate (Fig. 1a). Each mechanism is equipped with an encoder and a PID controller implemented on an Arduino Nano microcontroller (Fig. 1b, c), ensuring wire feed rate reproduction with an accuracy of 0.1 mm/s.



(a) (b)

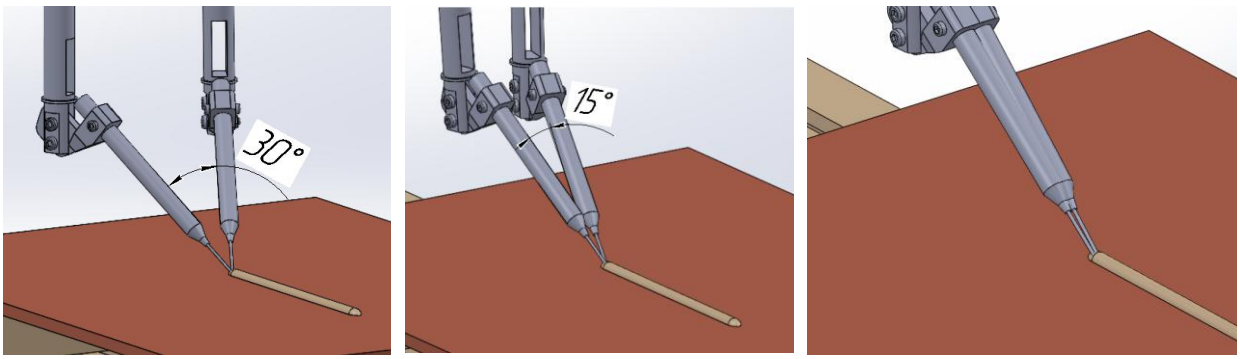
(c)

Fig. 1 Experimental setup for dual-wire electron beam additive manufacturing: **(a)** wire feed nozzles on adjustable holders; **(b)** general view of the experimental setup; **(c)** schematic diagram of the wire feed system

To investigate the effect of wire feeding geometry on the metal transfer mode, three configurations were considered: unilateral feeding with β = 30° (Fig. 2a), unilateral feeding with β = 15° (Fig. 2b), and parallel feeding with β = 0° (Fig. 2c), where β is the convergence angle between the nickel and titanium wire feed axes. At β = 0°, a specially designed single nozzle was used. The deposition process parameters are presented in Table 1.

Table 1 Deposition process parameters

№	Parameter	Value
1	Beam current, mA	20 → 10
2	Beam deflection frequency, Hz	250
3	Beam deflection pattern	Circle
4	Deposition speed, m/h	15
5	Nickel wire feed rate, mm/s	5.5
6	Titanium wire feed rate, mm/s	8.1
7	Nozzle inclination angle, α°	35
8	Wire convergence angle, β°	0 → 30



(a) (b) (c)

Fig. 2 Wire feeding configurations: **(a)** convergence angle β = 30°; **(b)** convergence angle β = 15°; **(c)** parallel feeding β = 0°

2.2. SPH modelling of the metal transfer process

To justify the effect of the convergence angle β on the metal transfer mode, SPH modelling of the wire melting process was performed for three configurations — β = 30°, 15° and 0° — accounting for surface tension forces, vapour pressure and thermocapillary convection (Marangoni effect). The SPH method represents a continuous medium as a set of discrete particles moving with the flow (Lagrangian approach), enabling effective modelling of free surface deformations, droplet and bridge formation during liquid metal transfer [13, 14].

The physical problem formulation was based on several assumptions: the material was characterised by constant thermophysical properties, and the heat source was applied directly to the sample surface with a Gaussian energy distribution. The computational domain was divided into a liquid phase Ωl (molten metal) and a solid phase Ωs (unmelted substrate and wire).

The melt was treated as an incompressible Newtonian fluid. The melt dynamics were described by the continuity equation (1) and the Navier–Stokes equation (2):

$$\frac{d\rho}{dt} = -\rho(\nabla \cdot \mathbf{u}) \tag{1}$$

where ρ is the density, u – is the velocity vector.

$$\rho\left(\frac{\partial \mathbf{u}}{\partial t} + (\mathrm{u} \cdot \nabla)\mathbf{u}\right) = -\nabla p + \nabla \cdot (\mu \nabla \mathbf{u}) + \rho \mathbf{g} \tag{2}$$

where ρ is the density, u is the velocity vector, p is the pressure, μ is the dynamic viscosity, g is the gravitational acceleration.

The thermal balance was described by the transient heat conduction equation with an effective heat capacity accounting for the latent heat of fusion over the solidus–liquidus temperature range:

$$\rho c_p^{eff}\left(\frac{\partial T}{\partial t} + (\mathrm{u} \cdot \nabla)T\right) = \nabla \cdot (k \nabla T) \tag{3}$$

where T is the temperature, c_p^{eff} is the effective specific heat capacity, k is the thermal conductivity

The heat input from the electron beam was modelled as a concentrated heat source with a Gaussian power distribution on the sample surface:

$$q_{src}(\mathbf{r}, t) = \eta_0 \frac{3Q_0}{\pi r_{src}^2} \exp\left[-\frac{3}{r_{src}^2}\left(\left(x - x_{src}(t)\right)^2 + \left(y - y_{src}(t)\right)^2\right)\right] \tag{4}$$

where η_0 is the heat transfer intensity, Q_0 is the heat source power, r_{src} is the heat source radius, $(x_{src}(t), y_{src}(t))$ are the coordinates of the heat source centre.

Heat losses due to evaporation, convective and radiative heat exchange with the surrounding environment were accounted for at the free surface of the melt. Evaporation losses and vapour pressure force were described by the following empirical expressions [15]:

$$\mathbf{f}_{evp} = -p_{evp}\mathbf{n} = -A_p p_a \, exp\left[-\frac{h_{evp}}{R}\left(\frac{1}{T} - \frac{1}{T_{evp}}\right)\right]\mathbf{n} \quad (5)$$

where p_{evp} is the vapour pressure, n is the surface normal, A_p is a coefficient depending on the ambient pressure (values range from 0.55 to 1), p_a is the evaporation constant, h_{evp} is the latent heat of evaporation, R is the universal gas constant, T_{evp} is the evaporation temperature, T is the temperature.

$$q_{evp} = \frac{A_q p_a h_{evp}}{\sqrt{2\pi MRT}} exp\left[-\frac{h_{evp}}{R}\left(\frac{1}{T} - \frac{1}{T_{evp}}\right)\right] \quad (6)$$

where M is the molar mass.

Convective and radiative heat exchange with the surrounding environment were accounted for using Newton–Richmann (7) and Stefan–Boltzmann (8) laws:

$$q_{env} = q_h(T - T_{env}), \quad (7)$$

$$q_{rad} = \sigma_B \varepsilon\left(T^4 - {T_{env}}^4\right), \quad (8)$$

where q_h is the heat transfer coefficient, σ_B is the Stefan–Boltzmann constant $\sigma_B \approx 5.67\times10^{-8}$ W/(m²·K⁴)), ε is the emissivity (ranging from 0 to 1), T is the temperature, T_{env} is the ambient temperature.

Surface phenomena — surface tension force and thermocapillary convection (Marangoni effect) — were represented as distributed body forces within a thin layer near the free surface. The surface tension force was defined as [16]:

$$\mathbf{f}_s = -\alpha(T)\kappa\mathbf{n} + (\mathbf{I} - \mathbf{nn})\nabla\alpha(T) \quad (9)$$

where $\alpha(T)$ is the temperature-dependent surface tension coefficient, κ is the surface curvature, **n** is the surface normal, **I** is the second-order identity tensor.

The first term described the normal component of the force (Laplace pressure), the second — the tangential component (Marangoni convection).

The developed heat and mass transfer model based on the SPH method has previously been applied to wire additive manufacturing simulations. In [17], the formation of a single deposited bead was considered, accounting for metal melting and solidification, surface tension and thermocapillary flows. A further development of the model is presented in [18], where the effect of vibration on surface tension, droplet formation and transfer mode during deposition was investigated. Thus, the model has been validated both for describing deposited material formation and for studying the influence of additional technological effects on melt dynamics.

Using the developed model, a series of numerical experiments was conducted. The computational domain included a substrate measuring 25×14×5 mm and two filler wires with a diameter of 1 mm, fed at an angle α = 35° to the substrate surface. The convergence angle β was set by rotating the feed axes by ±β/2 relative to the deposition plane; at β = 0° the wire axes are parallel, with a gap of 0.6 mm between their surfaces (Fig. 3).

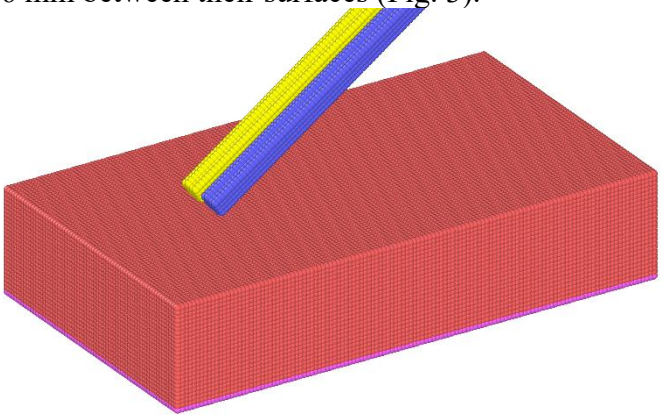


Fig. 3 Initial configuration of the computational domain at β = 0°: TN-1 substrate **(red)**, titanium **(yellow)** and nickel **(blue)** wires

Wire feeding was modelled by continuously adding solid material particles moving along the feed axis at a specified velocity — 8.1 mm/s for the titanium wire and 5.5 mm/s for the nickel wire. Particles of the substrate and unmelted wire sections formed the solid phase Ωs and did not participate in hydrodynamic motion. Upon heating above the liquidus temperature, a particle transitioned to the liquid phase Ωl; upon cooling below the solidus temperature, it returned to the solid phase.

The heat source (Eq. 4) with an effective power of 1800 W and a spot radius of 1 mm traversed the stationary substrate at a deposition speed of 4.2 mm/s; the source centre additionally moved in a circular path at a frequency of 250 Hz, corresponding to the circular deflection pattern of the electron beam. A process segment of approximately 4 s duration was simulated, during which a bead of ~19 mm length was formed (Fig. 4).

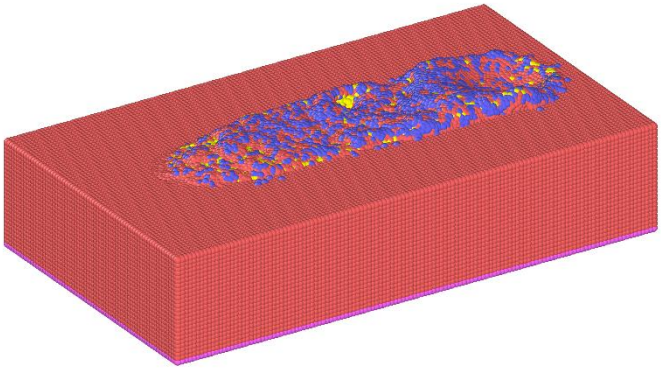


Fig. 4 Computational domain at the end of the simulation (t ≈ 4 s): deposited bead consisting of a mixture of nickel, titanium and remelted substrate material particles

Each particle was assigned a material label — TN-1K substrate, titanium wire or nickel wire — and an individual set of thermophysical properties (Table 2); for pairs of particles of dissimilar materials, the parameters were taken as arithmetic means. Thus, the difference in melting and transfer behaviour of the wires was entirely determined by the difference in their physical properties — melting temperatures, densities, thermal conductivities and surface tension coefficients.

Table 2 Thermophysical properties of materials used in the simulations

Property	Unit	NP2 (Ni)	VT1-00sv (Ti)	TN-1 (NiTi)
Solid/liquid phase density	kg/m³	8200 / 7700	4540 / 4110	8000 / 8000
Solidus/liquidus temperature	K	1610 / 1650	1933 / 1940	1513 / 1583
Thermal conductivity	W/(m·K)	60	20	65
Specific heat capacity solid/liquid	J/(kg·K)	500 / 650	650 / 830	456 /600
Latent heat of fusion	J/kg	$3.0\cdot10^5$	$3.0\cdot10^5$	$2.3\cdot10^5$
Heat of evaporation	J/kg	$3.7\cdot10^5$	$4.23\cdot10^5$	$4.0\cdot10^5$
Evaporation temperature	K	2970	3560	3000
$\sigma(T_{ref})$	N/m (T_{ref}, K)	1.743 (1728)	1.52 (1941)	1.53 (1603)
$d\sigma/dT$	N/(m·K)	$-3.1\cdot10^{-4}$	$-1.8\cdot10^{-4}$	$-2.6\cdot10^{-4}$
Dynamic viscosity	Pa·s	$4.7\cdot10^{-3}$	$3.0\cdot10^{-3}$	$7.24\cdot10^{-3}$
Molar mass	kg/mol	0.054	0.048	0.107

The initial inter-particle spacing Δ = 0.2 mm corresponded to approximately $2\cdot10^5$ particles in the initial configuration. The smoothing length was set to 1.5Δ for hydrodynamic operators and 3Δ for heat conduction and surface force operators.

To quantitatively assess the uniformity of component distribution, the chemical composition coefficient γ was introduced — defined as the ratio of the nickel wire mass flow rate to that of the titanium wire, determined through the feed rates V, cross-sectional areas F and

densities ρ of the components. The target value of γ for nitinol with a composition of 55 wt.% Ni / 45 wt.% Ti is 1.222; deviations from this value characterise the degree of chemical inhomogeneity of the alloy.

For the analysis of component distribution, a post-processing algorithm was applied to the simulation results. The longitudinal cross-section of the deposited bead in its central part was discretised into rectangular cells C_{ij} defined along the x, y and z axes:

$$G = \{(x, y, z) |\ x \in [x_{min}, x_{max}], y \in [y_{min}, y_{max}], z \in [z_{min}, z_{max}]\} \quad (10)$$

A two-dimensional grid was then constructed on the longitudinal cross-section (x–z):

$$G\Omega = \left\{ \begin{matrix} (x_i, z_j) |\ x_i = \Delta x \cdot i, i = \overline{0, M}, \Delta x = \dfrac{x_{max} - x_{min}}{M}; \\ z_j = \Delta z \cdot j, j = \overline{0, N}, \Delta z = \dfrac{z_{max} - z_{min}}{N} \end{matrix} \right\} \quad (11)$$

For each cell $[x_i, x_{i+1}) \times [z_j, z_{j+1}) = C_{ij}$, the number of particles of each material falling into the cell was calculated:

$$n_{ij}^k = \sum_{p \in G} \chi_p^k \theta_{ij}\,, k = 1 \ldots n_{mat} \quad (12)$$

where n_{mat} is the number of materials (in this case 3: titanium, nickel, nitinol), χ_p^k is the material indicator, θ_{ij} is the cell membership indicator, n_{ij}^k is the number of particles of material k falling into cell C_{ij}.

The total number of particles falling into the cell is then:

$$n_{ij}^{all} = \sum_{k=1}^{n_{mat}} n_{ij}^k \quad (13)$$

Each field was then smoothed using a Gaussian filter:

$$n_{ij}^{k,(s)} = G_{ij}^{\sigma} \cdot n_{ij}^k \quad (14)$$

where $n_{ij}^{k,(s)}$ is the smoothed concentration field, G_{ij}^{σ} is the Gaussian filter.

$$G_{ij}^{\sigma} = \frac{1}{Z} exp\left(-\frac{1}{2}\left[\left(\frac{i}{\sigma_x}\right)^2 + \left(\frac{j}{\sigma_z}\right)^2\right]\right) \quad (15)$$

where $\sigma_x = \frac{h}{\Delta x}$ is the smoothing width along x, $\sigma_z = \frac{h}{\Delta z}$ is the smoothing width along z, Z is the normalisation coefficient such that $\sum_{ij} G_{ij}^{\sigma} = 1$, i and j are the cell indices.

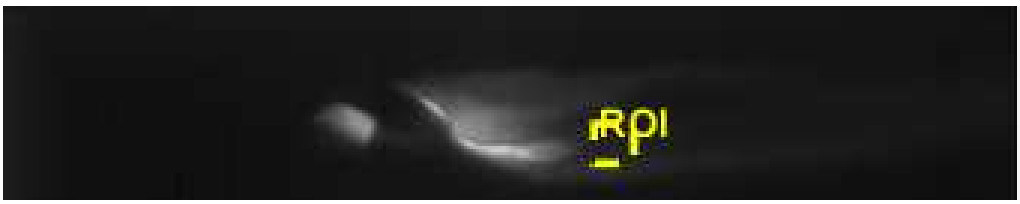
The algorithm output was a colour map of material distribution, where each colour shade corresponded to a numerical value of the chemical composition coefficient $\gamma = F_{Ni}/F_{Ti}$, characterising the local nickel-to-titanium ratio within the deposited bead volume.

2.3. High-speed videography and optical flow analysis

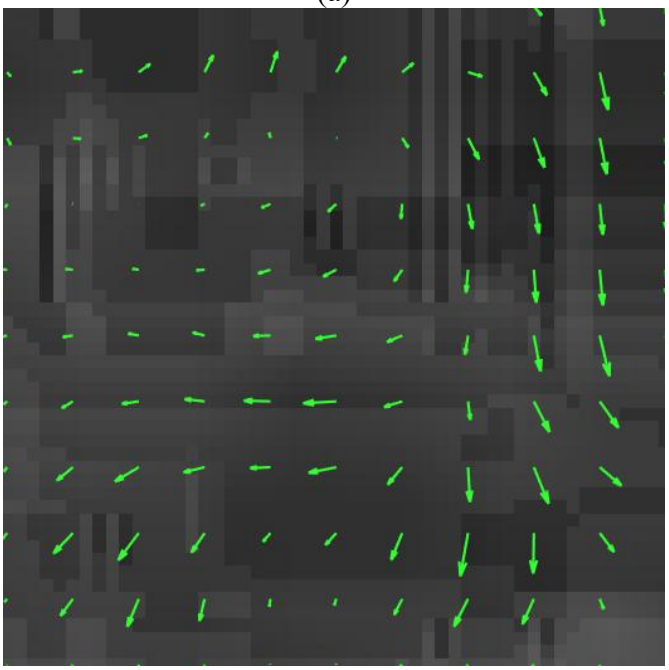
The simulation results were verified by high-speed videography (VideoSprint, 2000 fps) through the vacuum chamber viewport. The intensity of convective mixing was assessed from the recordings using a developed MATLAB algorithm within a region of interest (ROI) in the vicinity of the electron beam interaction zone (Fig. 5a).

Prior to analysis, each frame underwent pre-processing: contrast-limited adaptive histogram equalisation (CLAHE) was applied to enhance local contrast, followed by gamma correction to brighten shadows and an unsharp mask filter to accentuate boundaries. Pixels brighter than a defined threshold were excluded from the analysis as containing no informative gradients.

The convective velocity field was computed using the Farneback optical flow method with pyramidal frame decomposition, an averaging window of 35 pixels and a 5×5 polynomial approximation (Fig. 5b). The obtained velocity vectors were converted from pixels to millimetres per second using a scale factor determined from the known wire diameter in the recording. The mean and maximum convection velocities were calculated over the valid pixels within the ROI.



(a)



(b)

Fig. 5 *High-speed video recording processing using optical flow method:* ***(a)*** *region of interest (ROI) for liquid metal flow analysis;* ***(b)*** *velocity vector field*

At the final stage, the Péclet number (*Pe)*, convective homogenisation time (τ_{conv}) and diffusive homogenisation time (τ_{diff}) were calculated from the obtained mean convection velocity *V* using the following expressions:

$$Pe = V \cdot \frac{L}{D}, \tag{16}$$

$$\tau_{conv} = \frac{L}{V}, \tag{17}$$

$$\tau_{diff} = \frac{L^2}{D}, \tag{18}$$

where L is the characteristic melt pool size (5 mm), D is the liquid metal diffusion coefficient (10^{-9} m²/s).

Comparison of τ_{conv} with the liquid phase lifetime allowed assessment of whether convection ensures complete mixing of the melt prior to the onset of solidification.

2.4. Metallographic investigation

For metallographic investigation, the samples were cut using a sectioning machine and mounted in a Buehler SimpliMet 1000 metallographic press. After mounting, the specimens were ground on abrasive paper with grit sizes ranging from P80 to P1000 and polished. To reveal the microstructure, the polished samples were etched with Beraha reagent. The microstructure was examined using a Zeiss Observer Z1m optical microscope at ×50 magnification with panoramic image stitching.

To assess the chemical homogeneity throughout the deposited wall volume, HV5 hardness measurements were performed across the wall cross-section in three zones — lower, middle and upper. The uniformity of hardness distribution was used as an indirect indicator of chemical composition homogeneity: zones of elevated hardness correspond to regions with increased intermetallic phase content, indicative of local deviations from stoichiometric composition.

3. Results

3.1. SPH simulation results and chemical composition coefficient distribution

The SPH simulation results for the three wire convergence angle configurations — β = 30°, 15° and 0° — are presented in Fig. 6 alongside frames from high-speed videography.

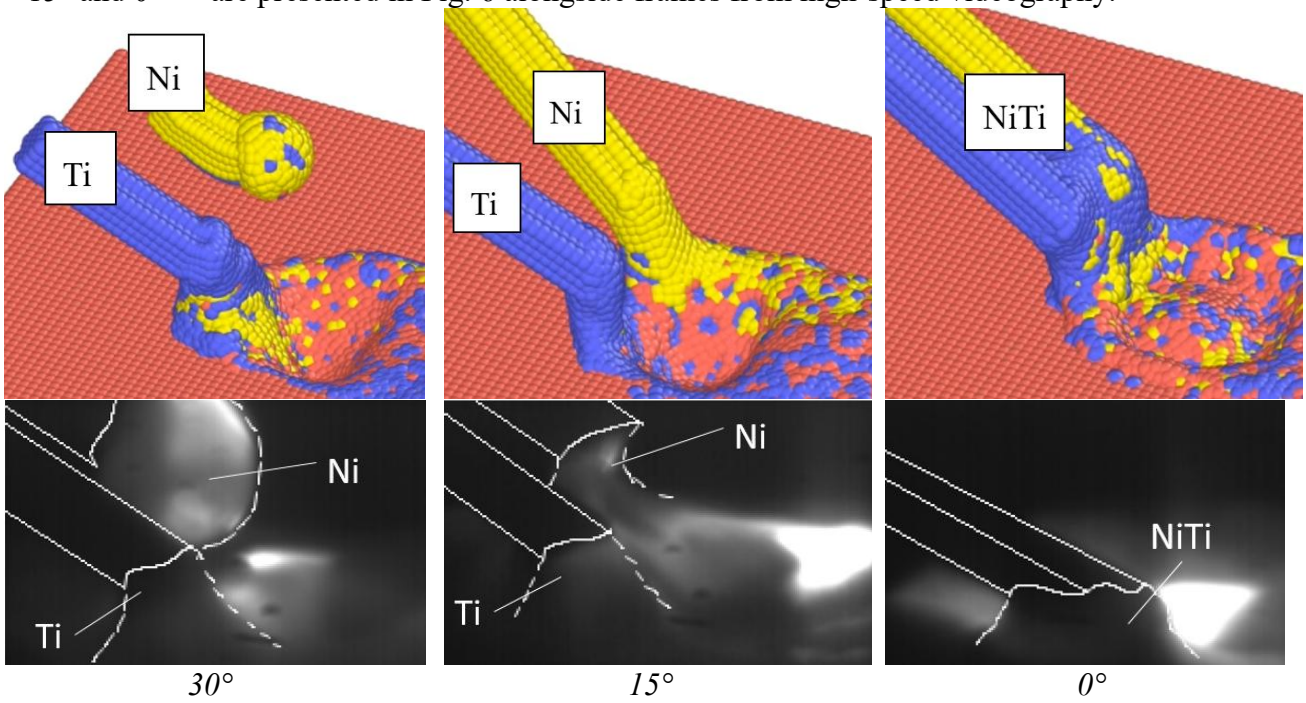


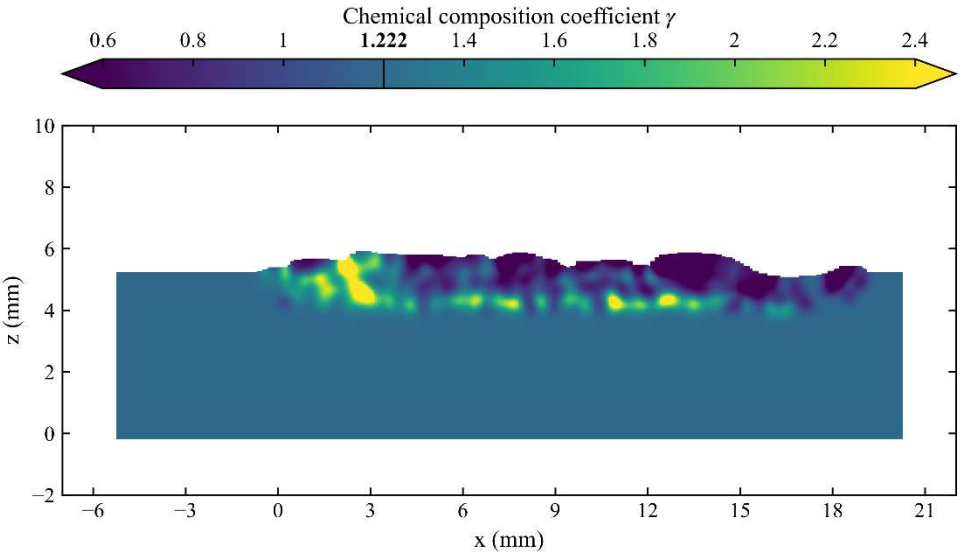
Fig. 6 Metal transfer modes at different wire convergence angles: SPH simulation results and high-speed videography frames

At β = 30°, the simulation results for single bead deposition reveal unstable droplet transfer of the nickel wire into the melt pool: a large droplet formed at the wire tip, periodically detaching and entering the melt pool. The titanium wire maintained stable bridge transfer throughout. High-speed videography confirmed this behaviour: the asynchronous transfer of components led to periodic local nickel deficiency in the melt pool, creating conditions for the formation of titanium-enriched zones.

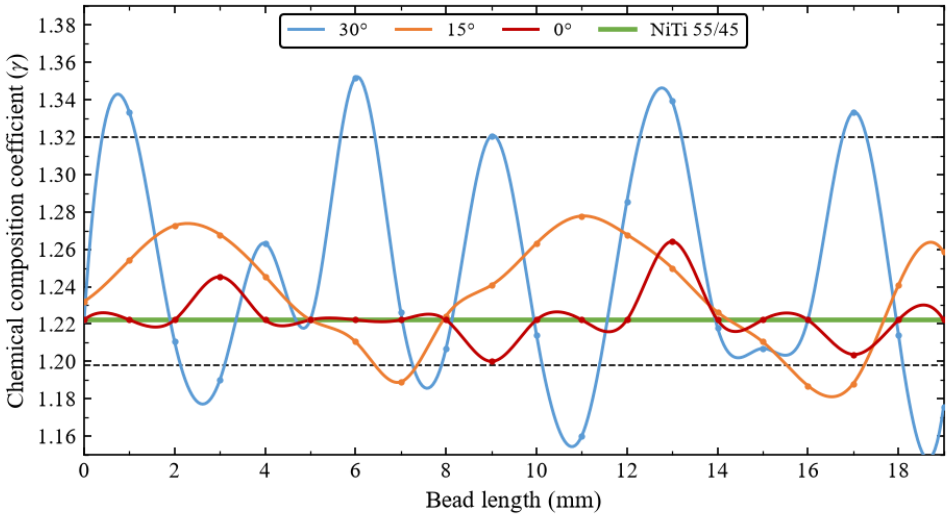
At β = 15°, the numerical simulation results show a more uniform distribution of nickel and titanium particles across the bead surface compared to β = 30°; however, mixing still occurred directly within the melt pool. A distinctive feature of this configuration was the formation of two separate transfer bridges — one from each wire — confirmed by both simulation results and high-speed videography analysis. The presence of two independent transfer bridges meant that the components entered the melt pool separately, with mixing driven exclusively by the electron beam deflection pattern generating thermocapillary flows. High-speed videography additionally revealed periodic transitions of the nickel wire to droplet transfer mode that were not visually apparent during process observation, indicating that mixing quality depended solely on a single controlling parameter — the beam deflection mode.

At parallel feeding (β = 0°), the melting and mixing kinetics changed fundamentally. Prior to entry into the main melt pool, active wetting of the wire contact surfaces was observed, along with preliminary mixing in the liquid phase. As a result, nickel and titanium entered the melt pool not separately but as an already partially formed melt, establishing a single stable transfer bridge. This result was confirmed by both simulation and high-speed videography.

To assess the uniformity of component distribution based on the simulation results, chemical composition coefficient γ distribution maps were constructed on longitudinal computational cross-sections. An example of a computational cross-section with a nickel and titanium particle distribution map is shown in Fig. 7a; the distribution of coefficient γ along the bead length for all three configurations is shown in Fig. 7b.



(a)



(b)

Fig. 7 SPH simulation results: **(a)** nickel and titanium particle distribution map on the computational cross-section; **(b)** chemical composition coefficient γ distribution along the bead length for all three configurations

At β = 30°, the greatest scatter in γ values was observed: the mean deviation from the target value of 1.222 was 3.6%, the maximum reached 10.6%, and the value range was 1.16–1.35. At β = 15°, the mean deviation decreased to 2.2%, the maximum to 4.6%, and the range narrowed to 1.19–1.28. Parallel feeding (β = 0°) yielded the lowest scatter: the mean deviation was 0.4%, the maximum 3.4%, with γ values ranging from 1.20 to 1.26.

3.2 High-speed videography and optical flow analysis

To verify the simulation results experimentally, high-speed video recordings were analysed using the optical flow method. For each of the three configurations, the liquid phase lifetime, convective homogenisation time, Péclet number and mean convection velocity were determined. The results are presented in Table 3.

Table 3 Results of high-speed video recording analysis of the deposition process

Wire convergence angle, °	Liquid phase lifetime, s	Convective homogenisation time, s	Péclet number	Mean convection velocity, mm/s
30	0.465	0,435	57461.3	11.49
15	0.588	0,417	59931.3	11.99
0	1.040	0,346	72165.8	14.43

As the convergence angle decreased from 30° to 0°, the liquid phase lifetime increased from 0.465 s to 1.040 s, while the mean convection velocity increased from 11.49 to 14.43 mm/s. The increase in liquid phase lifetime at β = 0° is attributed to the fact that melting and preliminary mixing of the components began prior to entry into the melt pool, forming a single melt of greater volume.

In all three configurations, the convective homogenisation time was shorter than the liquid phase lifetime, indicating that complete mixing of the components prior to solidification is fundamentally achievable at any of the considered angles. However, at β = 30° the time margin was only ~7%, whereas at β = 0° it reached ~67%, providing substantially more favourable conditions for homogeneous chemical composition formation. The high Péclet number (~10^4) in all configurations confirms the dominance of convective over diffusive transport — the chemical composition homogeneity is determined exclusively by melt pool hydrodynamics. The maximum Pe value at β = 0° confirms the most intensive convective mixing under parallel wire feeding. A comparative diagram of the investigated parameters is presented in Fig. 8.

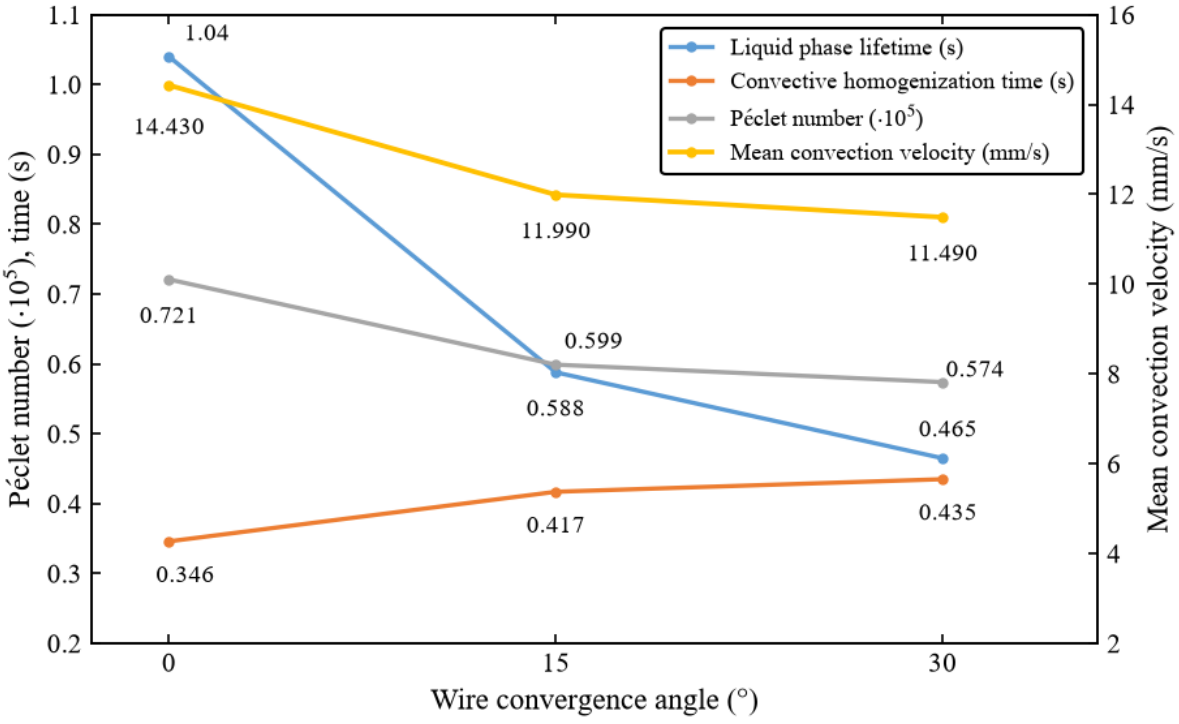
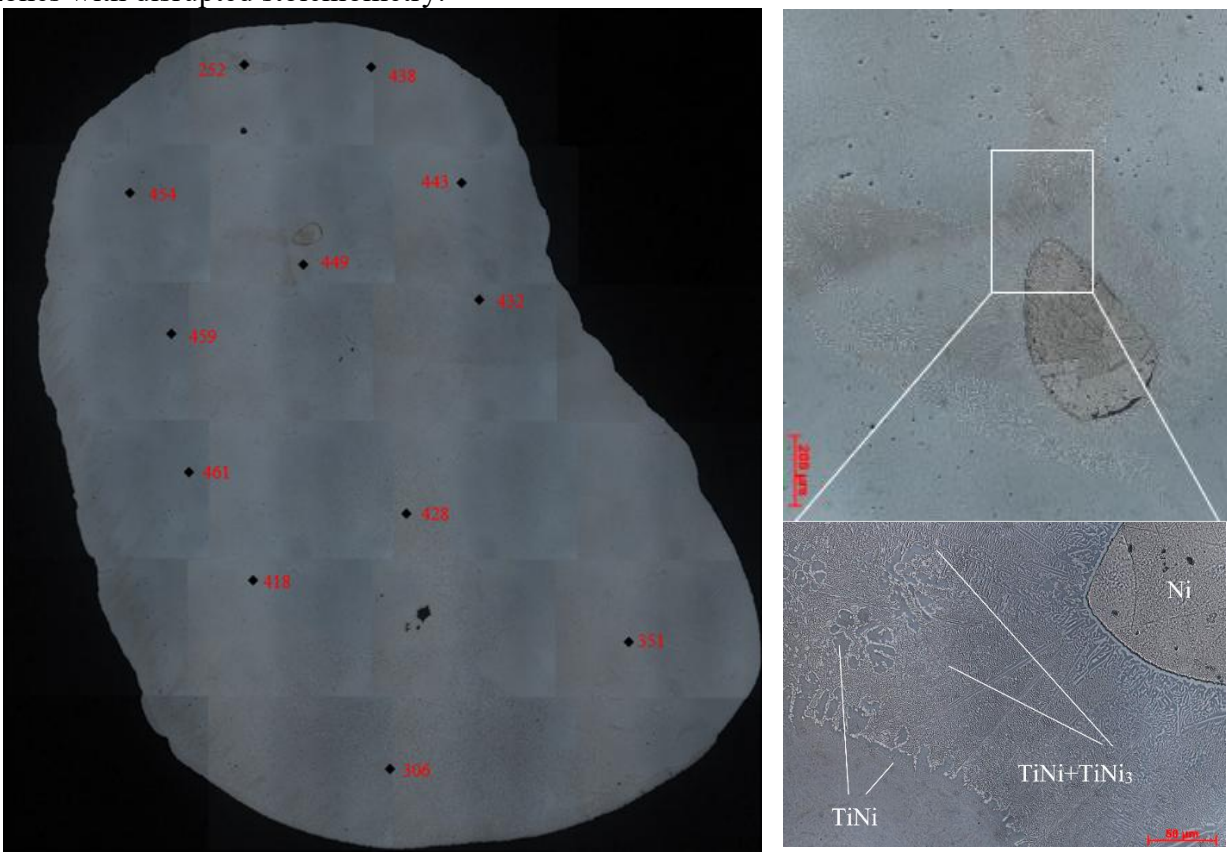


Fig. 8 Liquid phase lifetime, convective homogenisation time, Péclet number and mean convection velocity as a function of wire convergence angle

3.3 Metallographic analysis and hardness distribution

The sample produced at β = 30° exhibited the greatest structural inhomogeneity — three characteristic zones of structural and phase inhomogeneity were identified (Fig. 9a). In the middle section, nickel supersaturation was caused by feed instability and incomplete melting of the nickel wire, leading to the formation of fine TiNi+$TiNi_3$ eutectic in regions adjacent to the unmelted wire, with a hardness of 449 HV5. In the lower section, the structure comprised supersaturated TiNi with secondary $TiNi_3$ precipitates, metastable Ti_3Ni_4/Ti_2Ni_3 phases and TiNi+$TiNi_3$ eutectic along grain boundaries, with a hardness of 428 HV5. In the upper section, slight titanium supersaturation

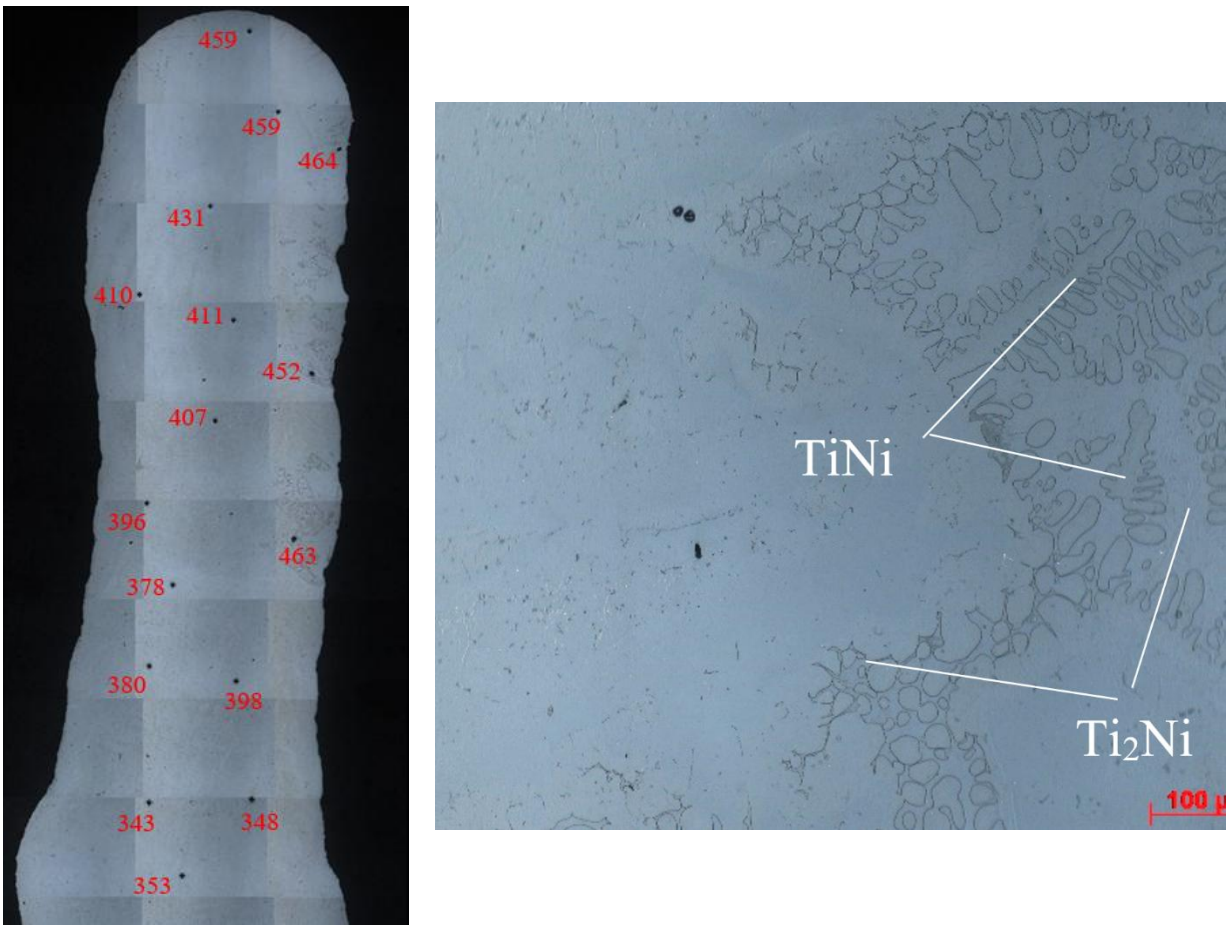
was observed, with Ti_2Ni interlayers forming along TiNi grain boundaries and a reduced hardness of 252 HV5. The microstructure of local inhomogeneities is shown in Fig. 9b. Thus, droplet transfer of the nickel wire at β = 30° led to periodic local nickel deficiency and the formation of zones with disrupted stoichiometry.



(a) (b)

Fig. 9 Sample produced at β = 30°: **(a)** external appearance with HV5 hardness distribution; **(b)** microstructure of local inhomogeneities

In the sample produced at β = 15°, chemical inhomogeneity in the central section was prevented. Nevertheless, local titanium-supersaturated zones with a hardness of 452–464 HV5 and a TiNi+Ti_2Ni structure were identified in the upper half of the sample (Fig. 10a). This inhomogeneity is presumably attributable to periodic transitions of the nickel wire to droplet transfer mode, recorded during high-speed videography, which led to local compositional deviations under separate two-bridge mixing conditions. The microstructure of the identified inhomogeneities is shown in Fig. 10b.

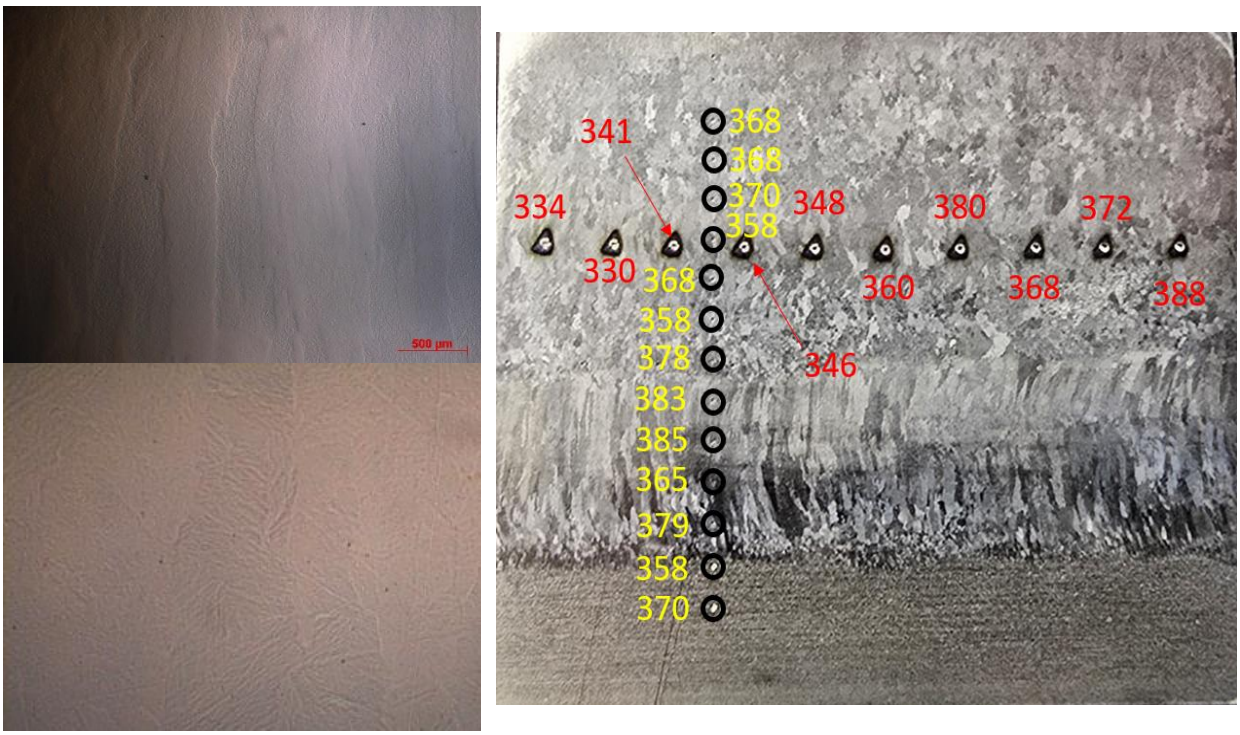


(a) (b)

Fig. 10 Sample produced at β = 15°: **(a)** external appearance with HV5 hardness distribution; **(b)** microstructure of local inhomogeneities

In the sample produced at parallel wire feeding (β = 0°), structural inhomogeneity was almost entirely suppressed: only a few zones with minor titanium supersaturation were detected throughout the sample. The sample structure is uniform, comprising a NiTi matrix with traces of martensitic transformation (Fig. 11a). The reduced etchability of the sample compared to previous series indirectly indicates the absence of significant deviations from NiTi stoichiometry. Epitaxial grain growth characteristic of layer-by-layer additive manufacturing was observed (Fig. 11b).

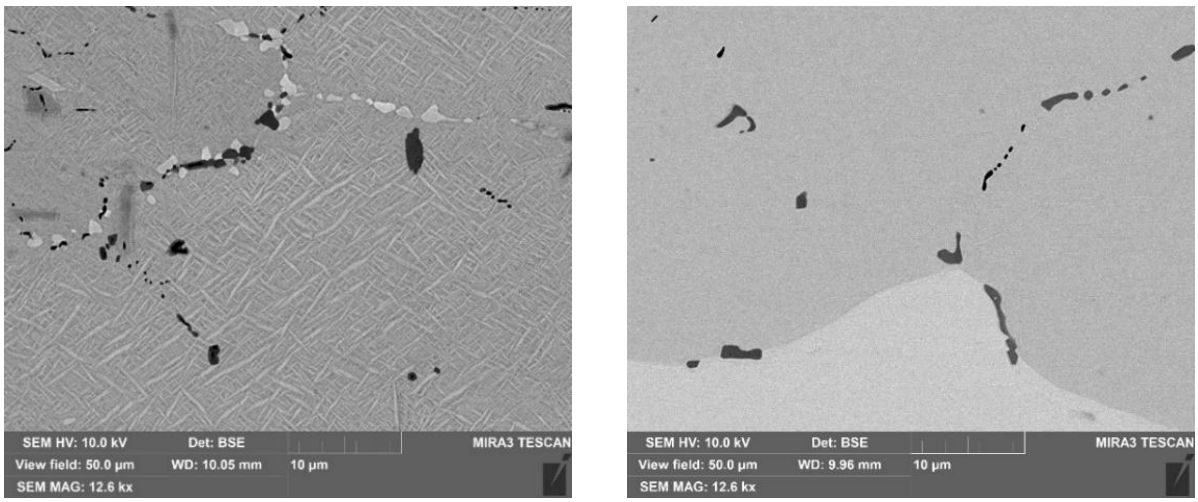
Hardness distribution was investigated in two directions — along the length and across the height of the sample. In the longitudinal direction, hardness values increased from 330–346 HV5 in the lower section to 372–388 HV5 in the upper section, attributed to the thermal cycle of layer-by-layer deposition: upper layers cool more rapidly and are not subjected to reheating, forming supersaturated TiNi with dispersed metastable Ti_3Ni_4/Ti_2Ni_3 phase precipitates. Lower layers undergo multiple thermal cycles during subsequent layer deposition, leading to partial decomposition of metastable phases and reduced hardness. In the transverse direction (bottom to top), hardness values ranged from 358–385 HV5 without a pronounced gradient, indicating uniform hardness distribution in this direction. Thus, the hardness of the sample produced at β = 0° is uniform in the transverse direction and varies systematically in the longitudinal direction, collectively confirming the chemical and structural homogeneity of the synthesised nitinol throughout the entire bead volume.



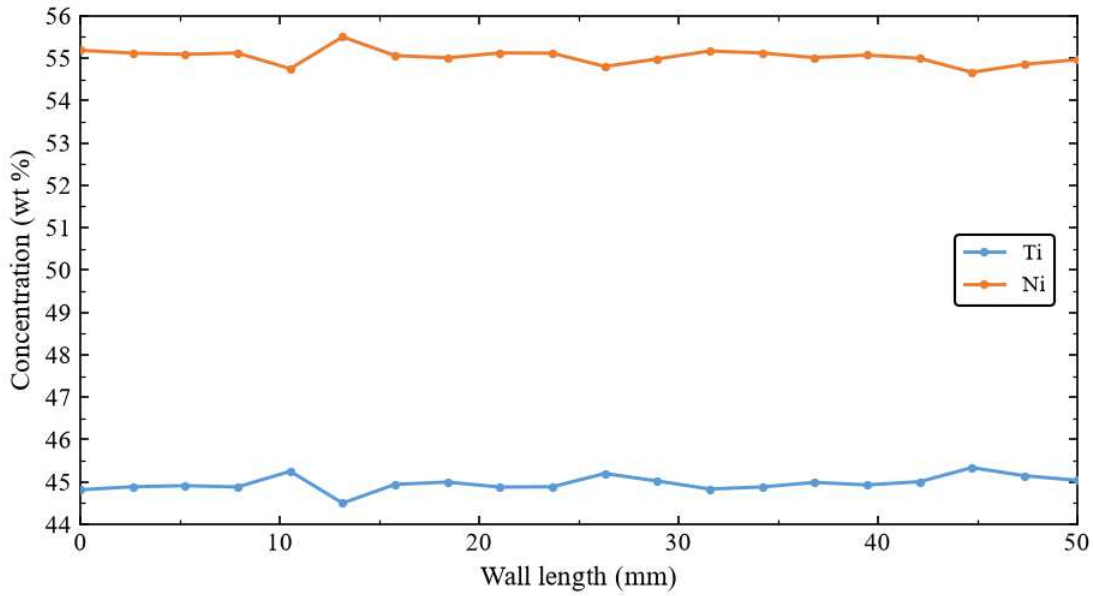
(a) (b)

Fig. 11 Sample produced at β = 0°: **(a)** NiTi matrix microstructure; **(b)** external appearance with HV5 hardness distribution

SEM analysis of the sample produced at β = 0° confirmed the homogeneity of the NiTi matrix. Uniformly distributed dispersed precipitates of secondary excess phases of the Ti_3Ni_4/Ti_2Ni_3 type with acicular morphology were identified within the grain interior, along with two types of non-metallic inclusions: carbonitrides arranged in chains along crystallite boundaries, and a grey Ti_4Ni_2O oxide phase (Fig. 12a). The most probable cause of these inclusions is impurities present in the initial filler wires. Analysis of the chemical composition distribution throughout the sample volume (Fig. 12b) confirmed minor nickel supersaturation not exceeding 0.5 wt.%.



(a)



(b)

Fig. 12 SEM analysis of the sample produced at β = 0°: **(a)** microstructure with dispersed phase precipitates and non-metallic inclusions; **(b)** chemical composition distribution along the sample length

4. Discussion

The results demonstrate that the metal transfer mode is the determining factor of chemical homogeneity in dual-wire EBAM of nitinol. This conclusion is consistent with the findings of Ze Pu et al. [6], who also observed chemical composition inhomogeneity in the lower layers of the deposited wall near the substrate during dual-wire EB-DED of nitinol, attributing it to instability of the filler wire melting process. However, in that study, homogeneous composition was achieved in the middle and upper sections of the wall without systematic investigation of the effect of wire feeding geometry on the transfer mode. The present work addresses this gap, demonstrating that the nozzle convergence angle β is a controlling parameter enabling deliberate transition of the transfer mode from droplet to bridge.

A recent study on dual-wire EB-DED of nitinol with controlled wire feed rate ratio [19] confirms the feasibility of synthesising nitinol with adjustable chemical composition and good mechanical properties — elongation up to 11%. The authors attribute structural inhomogeneity to the thermal history of the process, but do not consider metal transfer hydrodynamics as an independent factor. The present work demonstrates that asynchronous droplet transfer of the nickel wire at $\beta \geq 30°$ is the primary cause of local zones with disrupted stoichiometry, leading to the formation of brittle intermetallic phases Ti_2Ni and $TiNi_3$.

Existing studies on dual-wire nitinol synthesis [6, 19] rely on the analysis of already deposited samples, from which the metal transfer behaviour can only be inferred indirectly. The mathematical model employed in this work enabled direct observation of component melting and transfer: bridge transfer disruption and droplet detachment, formation of two separate transfer bridges, and preliminary mixing of components under parallel feeding — phenomena that are difficult to distinguish by visual process observation. The simulated transfer modes are consistent with high-speed videography data for all three configurations, and the calculated γ coefficient maps are consistent with metallographic analysis results. This enables the model to be used for selecting wire feeding geometry at the process design stage without conducting a series of physical experiments.

The tendency towards increasing hardness from lower to upper layers identified in this work is consistent with the findings of Guimarães et al. [20], who also observed microstructural inhomogeneity along the height of nitinol deposits produced by electron beam additive manufacturing, attributing it to the preheating effect of lower layers during subsequent deposition. In the present work, this effect is explained from a thermokinetic perspective: upper layers form supersaturated TiNi with dispersed metastable Ti_3Ni_4/Ti_2Ni_3 phase precipitates, while lower layers undergo multiple thermal cycles leading to their partial decomposition and coagulation.

The presence of non-metallic inclusions — carbonitrides and Ti_4Ni_2O oxide phase — in the sample produced at $\beta = 0°$ is consistent with data reported by other authors on EBAM of nitinol and is attributed to impurities in the initial filler wires. The vacuum environment of the process substantially limits oxidation compared to laser-based methods [10], but does not entirely prevent oxygen entrapment during solidification in the presence of wire impurities.

The key original result of the present work is the establishment of the dependence of the metal transfer mode on the wire convergence angle β and the demonstration that transition to parallel feeding ($\beta = 0°$) fundamentally changes the component mixing mechanism: instead of separate entry of nickel and titanium into the melt pool, their preliminary mixing is ensured at the melting stage. This approach has no direct analogues in the published literature on dual-wire nitinol synthesis and may be applied to the synthesis of other binary alloys with substantially differing surface tension coefficients of the components.

5. Conclusion

The present work investigates the mechanisms of local chemical inhomogeneity formation in dual-wire electron beam additive manufacturing of nitinol and identifies the technological conditions for their suppression.

1. The developed heat and mass transfer model successfully reproduced all three observed metal transfer modes and their transition with varying convergence angle β, confirmed by high-speed videography. The γ coefficient maps constructed from the simulation results enabled quantitative assessment of bead chemical inhomogeneity prior to metallographic investigation.
2. The convergence angle β determines the metal transfer mode: at $\beta \geq 30°$, droplet transfer of the nickel wire was observed with a maximum γ deviation of 10.6%; at $\beta = 15°$, two separate transfer bridges formed with mixing driven solely by beam deflection, mean γ deviation — 2.2%; at $\beta = 0°$, a single stable bridge formed with preliminary mixing of components prior to melt pool entry, reducing the mean γ deviation to 0.4%.
3. At $\beta = 0°$, the liquid phase lifetime increases to 1.040 s, and the homogenisation time margin reaches ~67% compared to ~7% at $\beta = 30°$. The Péclet number (~10^4) in all configurations confirms the dominance of convection over diffusion.
4. Metallographic analysis showed that at $\beta = 0°$ the structure is uniform, the NiTi matrix is homogeneous, transverse hardness ranges from 358 to 385 HV5, and longitudinal hardness increases systematically from 330 to 388 HV5 due to the thermal cycle of layer-by-layer deposition.

Statements and Declarations

Funding

This work was supported by the Ministry of Science and Higher Education of the Russian Federation. The research concept, experimental setup development, physical deposition experiments and metallographic analysis were carried out at the National Research University "Moscow Power Engineering Institute" (MPEI) under State Assignment No. FSWF-2026-0004 "Development of a scientifically grounded methodology for designing the blade apparatus of advanced high-power turbomachines based on the application of functionally graded materials and coatings". The development of the heat and mass transfer model, numerical experiments and analysis of simulation results were carried out at Perm National Research Polytechnic University (PNRPU) under State Assignment No. FSNM-2024-0003 "Development of scientific and technological foundations for the formation of a material-structure system with special properties based on hybrid additive technologies".

Competing Interests

The authors have no relevant financial or non-financial interests to disclose.

Author Contributions

All the authors contributed equally to the work.

References

1. Motzki P, Seelecke S (2021) Industrial applications for shape memory alloys. Shape Memory Superelast. https://doi.org/10.1016/B978-0-12-803581-8.11723-0

2. Kollerov MYu, Gusev DE, Gurtovaya GV, Ruchina NV, Gvozdeva ON (2015) Funktsional'nye materialy s effektom pamyati formy [Functional materials with shape memory effect]. Moscow, 161 p. [In Russian]

3. Otsuka K, Wayman CM (1998) Shape memory materials. Cambridge University Press, Cambridge, 284 p

4. Frenzel J, Zhang Z, Neuking K, Eggeler G (2004) High quality vacuum induction melting of small quantities of NiTi shape memory alloys in graphite crucibles. J Alloys Compd 28:214–223

5. Senin A, Pasechnik AYu (2021) Tekhnologicheskie osobennosti vyplavki splava nitinol [Technological features of nitinol alloy smelting]. In: Metallurgiya XXI stoletiya glazami molodykh: Materialy VII Mezhdunarodnoy nauchno-prakticheskoy konferentsii [Metallurgy of the 21st century: Proceedings of the 7th International Scientific and Practical Conference]; 24–26 May 2021; Donetsk. DonNTU, Donetsk, pp 64–66. [In Russian]

6. Pu Z, Du D, Wang K, Liu G, Zhang D, Zhang H, Xi R, Wang X, Chang B (2022) Study on the NiTi shape memory alloys in-situ synthesized by dual-wire-feed electron beam additive manufacturing. Addit Manuf 56:102886. https://doi.org/10.1016/j.addma.2022.102886

7. Pu Z, Chang B (2022) Control of droplet transfer during in-situ synthesis of NiTi alloys by dual-wire electron beam additive manufacturing. J Phys Conf Ser 2369:012011. https://doi.org/10.1088/1742-6596/2369/1/012011

8. Li Z, Chang B, Cui Y, Zhang H, Liang Z, Liu C, Wang L, Du D, Chang S (2022) Effect of twin-wire feeding methods on the in-situ synthesis of electron beam fabricated Ti-Al-Nb intermetallics. Mater Des 215:110509. https://doi.org/10.1016/j.matdes.2022.110509

9. Dutkiewicz J, Rogal Ł, Kalita D, Kawałko J, Weglowski M, Kwieciński K, Śliwiński P, Danielewski H, Antoszewski B, Cesari E (2021) Microstructure, mechanical properties, and martensitic transformation in NiTi shape memory alloy fabricated using electron beam additive manufacturing technique. J Mater Eng Perform 31. https://doi.org/10.1007/s11665-021-06241-x

10. Elahinia M, Moghaddam NS, Andani MT, Amerinatanzi A, Bimber BA, Hamilton RF (2016) Fabrication of NiTi through additive manufacturing: a review. Prog Mater Sci 83:630–663

11. Kollerov MYu, Aleksandrov AV, Gusev DE, Sharonov AA (2012) Vliyanie shikhtovogo materiala i metoda vyplavki na strukturu i effekt zapominaniya formy slitkov splavov na osnove nicelyda titana [Effect of charge material and melting method on structure and shape

memory effect of nickel titanide alloy ingots]. Tekhnologiya Legkikh Splavov 2:87–93. [In Russian]

12. Anoshkin NF (1976) Zonal'naya khimicheskaya neodnorodnost' slitkov [Zonal chemical inhomogeneity of ingots]. Metallurgiya, Moscow, 240 p. [In Russian]

13. Trautmann M, Hertel M, Füssel U (2018) Numerical simulation of weld pool dynamics using a SPH approach. Weld World 62(5):1013–1020. https://doi.org/10.1007/s40194-018-0615-5

14. Russell MA, Souto-Iglesias A, Zohdi TI (2018) Numerical simulation of laser fusion additive manufacturing processes using the SPH method. Comput Methods Appl Mech Eng 341:163–187. https://doi.org/10.1016/j.cma.2018.06.033

15. Semak V, Matsunawa A (1997) The role of recoil pressure in energy balance during laser materials processing. J Phys D Appl Phys 30:2541–2552. https://doi.org/10.1088/0022-3727/30/18/008

16. Brackbill JU, Kothe DB, Zemach CA (1992) Continuum method for modelling surface tension. J Comput Phys 100:335–354. https://doi.org/10.1016/0021-9991(92)90240-Y

17. Davlyatshin RP, Gerasimov RM, Bayandin YV, Permyakov GL, Trushnikov DN (2021) Mathematical modeling the process of wire surfacing by the smoothed particle hydrodynamics method. J Phys Conf Ser 1730:012003

18. Davlyatshin RP, Perminov AV, Bayandin YV, Saucedo-Zendejo FR, Trushnikov DN (2023) Numerical modeling of vibration effects on the surface tension of a liquid drop in additive technologies with SPH. Comput Part Mech 10:911–928

19. Zhang H, Du D, Wang K, Chang B (2024) In-situ synthesis of NiTi shape memory alloys with tunable chemical composition and thermomechanical response by dual-wire-feed electron beam directed energy deposition. J Mater Sci Technol. https://doi.org/10.1016/j.jmst.2024.07.028

20. Guimarães RPM, Rauchdobler B, Pixner F, Mahdi A, Ferraz FMB, Poletti C, Enzinger N, Amancio-Filho ST (2024) The electron beam freeform fabrication of NiTi shape memory alloys. Part II: influence of the heat treatment on the superelastic behaviour. Proc Inst Mech Eng Part L J Mater Des Appl. https://doi.org/10.1177/14644207231184787